

NASA-TM-80683 19800019054

A Reproduced Copy
OF

Reproduced for NASA

by the

NASA Scientific and Technical Information Facility

LIBRARY COPY

MAY 16 1983

LANGLEY RESEARCH CENTER
LIBRARY, NASA
HAMPTON, VIRGINIA



Technical Memorandum 80683

FOCAL AXIS RESOLVER FOR OFFSET REFLECTOR ANTENNAS

R. F. SCHMIDT

(NASA-TM-80683) FOCAL AXIS RESOLVER FOR
OFFSET REFLECTOR ANTENNAS (NASA) 36 p
HC A03/MF A01 CSCL SEC

2025 RELEASE UNDER E.O. 14176

Unclassified
G3/32 25-301

MAY 1980

National Aeronautics and
Space Administration
Goddard Space Flight Center
Greenbelt, Maryland 20771



N80-27555 #

NASA
TECHNICAL MEMORANDUM 80683

FOCAL AXIS RESOLVER FOR OFFSET REFLECTOR ANTENNAS

R. F. SCHMIDT

MAY 1980

NATIONAL AERONAUTICS AND SPACE ADMINISTRATION
GODDARD SPACE FLIGHT CENTER
GREENBELT, MARYLAND 20771

FOCAL AXIS RESOLVER FOR OFFSET REFLECTOR ANTENNAS

R. F. SCHMIDT

ABSTRACT

This document describes electrical means for determining the focal axis of an offset reflector antenna whose physical rim is not coincident with the boundary of the electrical aperture. Even and odd sensing functions are employed in the focal region, leading to both amplitude and phase criteria for resolving a focal axis generally inclined with respect to the system axis. The analytical aspects of the problem are discussed, and an example related to a 4-meter Large-Antenna Multiple-Frequency Microwave Radiometer (LAMMR) is included. It is shown that the technique is useful for focal axis determination in mathematical simulations and in the physical world.

CONTENTS

	<u>Page</u>
ABSTRACT	iii
GLOSSARY OF NOTATION	viii
INTRODUCTION	1
THEORY	3
RADIATION PATTERN DATA	7
DUAL-ANGLE RESOLUTION	15
CONCLUSION	22
ACKNOWLEDGEMENTS	23
REFERENCES	24

APPENDIXES

Appendix

A-1 Rim and Aperture Boundaries

Page

A-1

ILLUSTRATIONS

<u>Figure</u>	<u>Page</u>
1 Single Offset Reflector Geometry	2
2 Wavefronts and Feeds in the Focal Region	4
3 Sum and Difference Channel Signals for Feed Rotation Angles $\beta \neq \theta_{FA}$	6
4 Squinted Beams of Feed Cluster ($\beta_1 = \beta_2 = 52^\circ$)	8
5 Sum and Difference Patterns ($\beta = 52^\circ$)	9
6 Sum and Difference Patterns ($\beta = 54^\circ$)	10
7 Sum and Difference Patterns ($\beta = 56^\circ$)	11
8 Difference Pattern Minima Versus Feed Cluster Rotation Angle (β)	13
9 Difference Pattern Minima Versus Feed Cluster Rotation Angle (β)	14
10 Sum and Difference Phase Patterns ($\beta = 52^\circ$)	16
11 Sum and Difference Phase Patterns ($\beta = 54^\circ$)	17
12 Sum and Difference Phase Patterns ($\beta = 56^\circ$)	18
13 Relative Phase Difference $ \psi_\Sigma - \psi_\Delta $, $\phi = 0^\circ$ Versus Feed Cluster Rotation Angle (β)	19
14 Relative Phase Difference $ \psi_\Sigma - \psi_\Delta $, $\phi = 0^\circ$ Versus Feed Cluster Rotation Angle (β)	20
15 Phase Relationships for Offset Paraboloid (ASM)	21
A-1 Offset Paraboloid	A-1

GLOSSARY OF NOTATION

F	focal point or focal length
Γ_Y	physical rim of surface
Γ_{AP}	hypothetical rim of aperture
θ_s	squint angle
K	beam deviation factor
Δ	lateral feed displacement (in context)
FA, EFA	focal axis, estimated focal axis
Σ, Δ	sum and difference patterns (EM field values)
θ, ϕ	angles of the spherical coordinate system
\bar{S}_i, \bar{S}_n	incident and reflected rays (vectors)
n	unit normal to a physical surface
PW	plane wave
CSW, ESW	condensing or expanding spherical wave
β_i	feed or feed pattern
Φ	phase center
ψ_i	phase angle or argument
α, β, γ	Euler angles
$\hat{i}_x, \hat{i}_y, \hat{i}_z$	Cartesian basis vectors
EM	electromagnetic
E_i	electromagnetic field or voltage due to a field
D	aperture diameter
D_3, R_3	feed diameter, radius
PSM	phase-sensing monopulse
ϵASM	errored amplitude-sensing monopulse
SW	spherical wave
$\delta\epsilon$	feed displacement vector ($x_\epsilon, y_\epsilon, z_\epsilon$)
$\overline{\pi L}$	discontinuous π -radian phase discontinuity
x_p, y_p, z_p	parent paraboloid coordinates
$\sigma_{\ell p}, \zeta_{\ell p}$	local radial and polar net variables
x_{1p}, y_{1p}	offset parameters of paraboloid
z_{1p}	axial displacement of paraboloid

FOCAL AXIS RESOLVER FOR OFFSET REFLECTOR ANTENNAS

R. F. Schmidt
Goddard Space Flight Center
Greenbelt, Maryland

INTRODUCTION

In both the mathematical simulation and the physical implementation of reflector antennas, the focal point (F) is of considerable interest. In many cases, knowledge of the focal point is sufficient and the focal axis is of no particular concern. Once a feed is situated at the focal point (of a paraboloid), feed rotation affects the amplitude distribution in the aperture plane, but the far-field radiation pattern is not squinted. In some cases, knowledge of the focal axis is also required. For example, rendering an annulus of the aperture ineffective by means of defocussing along the focal axis to achieve an increased beamwidth requires precise knowledge of the focal axis if beam squint is to be avoided. Angle-tracking systems (active or passive) ordinarily require determination of the focal axis as well. Examples of these can be found in textbooks and journal articles which discuss conical-scanning and monopulse angle-tracking techniques.

This memorandum is an outgrowth of offset reflector antenna studies associated with the Large-Antenna Multiple-Frequency Microwave Radiometer (LAMMR). Since the physical rim (Γ_Y) of the offset antenna is not, in general, congruent with the rim of the aperture (Γ_{AP}) but is, in fact, elliptical when the aperture is circular, the focal axis is not as obvious as it is for a symmetric or parent paraboloid. See Appendix A. For the latter, the perpendicular to the physical rim (Γ_Y) establishes the focal axis, and the focal point is found either directly by far-field techniques or indirectly by intermediate near-field techniques. See Reference 1. An estimate of the orientation of the focal axis of an offset antenna may be obtained from the central ray of an axially directed plane wave incident on the antenna. This approach is feasible for mathematical simulations where the equations of the offset antenna are known and the axis of the parent paraboloid is obvious. See Figure 1. In the physical realm, the symmetry plane of the offset antenna may be obvious, but the parent axis (\hat{f}_z) is not. An improved means for determining the focal axis in mathematical simulations is to carry out a complete focal region mapping procedure which provides isophotes, wavefronts, and time-average Poynting vectors. See Reference 2. Although expensive in computer cpu-time, three estimates of the focal axis are available via this approach. The physical counterpart of the preceding mapping is possible, but motivates an inquiry into simpler and more direct alternatives.

An iterative or indirect means for resolving the focal axis of an offset paraboloid which is applicable in both simulation and real worlds is to assume a candidate focal axis and rely on information obtained from successive feed displacement. This method was employed initially in the mathematical simulation of the antenna system at 37.0 and 91.0 GHz to study the effects of defocussing on LAMMR radiation pattern beamwidth. Since all axes except the focal axis will result in progressively larger secondary beam squint angles, approximately according to the equation

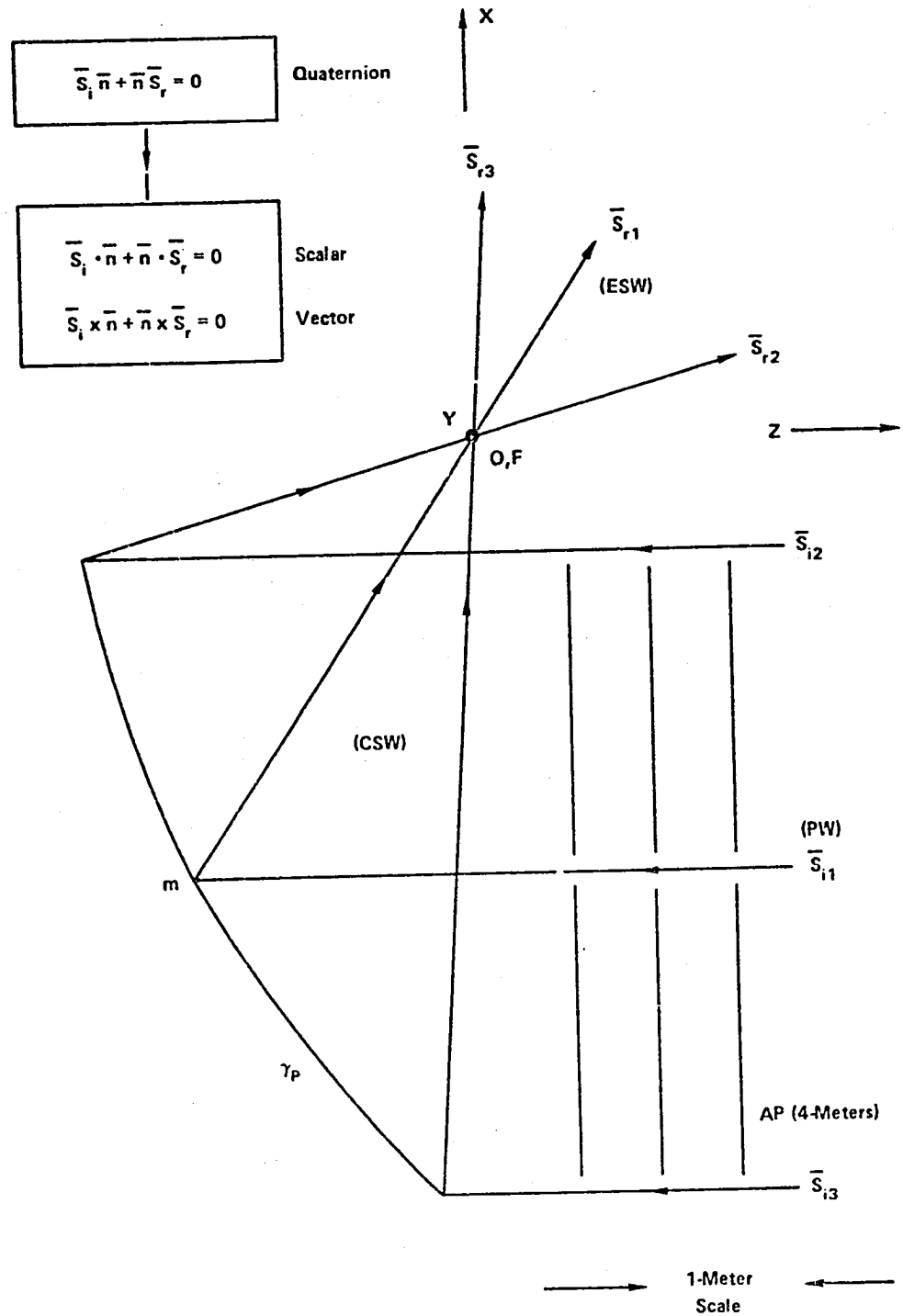


Figure 1. Single Offset Reflector Geometry.

$$\sin \theta_s = \frac{KA}{F} \quad (1)$$

where (Δ) is the feed displacement orthogonal to the focal axis, it is possible to converge on the focal axis by trial and error. One disadvantage of this approach is that both quadratic and linear phase gradients may be incurred in the aperture and these can significantly alter the beam shape. Misinterpretations concerning beam squint therefore occasionally occur and confuse the focal-axis updating process, at least temporarily. The direction (θ) of the main beam maximum becomes stationary as the process converges.

THEORY

The theory underlying the focal axis resolver presented in this memorandum is predicated on the assumption that the wavefronts of an offset paraboloid in the vicinity of the focal point (F) are essentially planar. See Reference 2. If the admission is made that the wavefronts on either side of the inclined Airy disc are converging spherical and diverging spherical waves, perhaps slightly asymmetric due to a finite F/D ratio (f-number), the representation of Figure 2 constitutes an idealization. Nevertheless, the iterative process to be described for determining a focal axis of an offset paraboloid still converges. A candidate focal axis is selected here also, based on a knowledge of geometric design parameters or a ray diagram.

In the theory of monopulse angle-tracking methods, the combination of a paraboloid and a feed cluster are said to comprise amplitude-sensing monopulse whereas an array by itself constitutes phase-sensing monopulse. See Reference 3, p. 70. Either configuration may be used to resolve the (θ, ϕ) angles of arrival of an essentially plane wave from a cooperative or non-cooperative target. A single pulse will effect the resolution, or continuous-wave tracking may be employed. A two-horn or four-horn feed cluster, and the associated monopulse (Σ) and (Δ) "comparator" network, may be introduced in the vicinity of the focus (F) as suggested by Figure 2. It is noted that the paraboloid, on reception, generates an inclined plane wave (approximately) in the vicinity of the focus and is not a part of the resolver mechanism. Furthermore, the focal axis which is to be determined is the one which corresponds to the situation shown in Figure 1, with an incident plane wave arriving along the focal axis of the parent paraboloid. The horn cluster therefore functions in a manner reminiscent of phase-sensing monopulse. In the present discussion, however, the inclined wave is stationary and the feed is rotated to obtain data that eventually resolve its direction of arrival. This should be contrasted with a conventional monopulse scenario in which the wave angle of arrival is changing continuously and the circuit generates a sum and difference signal pair to track the target continuously.

Initially assume that only the one spatial angle (θ) of Figure 2 is to be resolved. That is, either delete feeds \mathcal{F}_3 and \mathcal{F}_4 , temporarily, or declare that the comparator is a four-hybrid type which adds the outputs of \mathcal{F}_1 to \mathcal{F}_3 and those of \mathcal{F}_2 to \mathcal{F}_4 . This hybrid finally forms the sum and difference signals

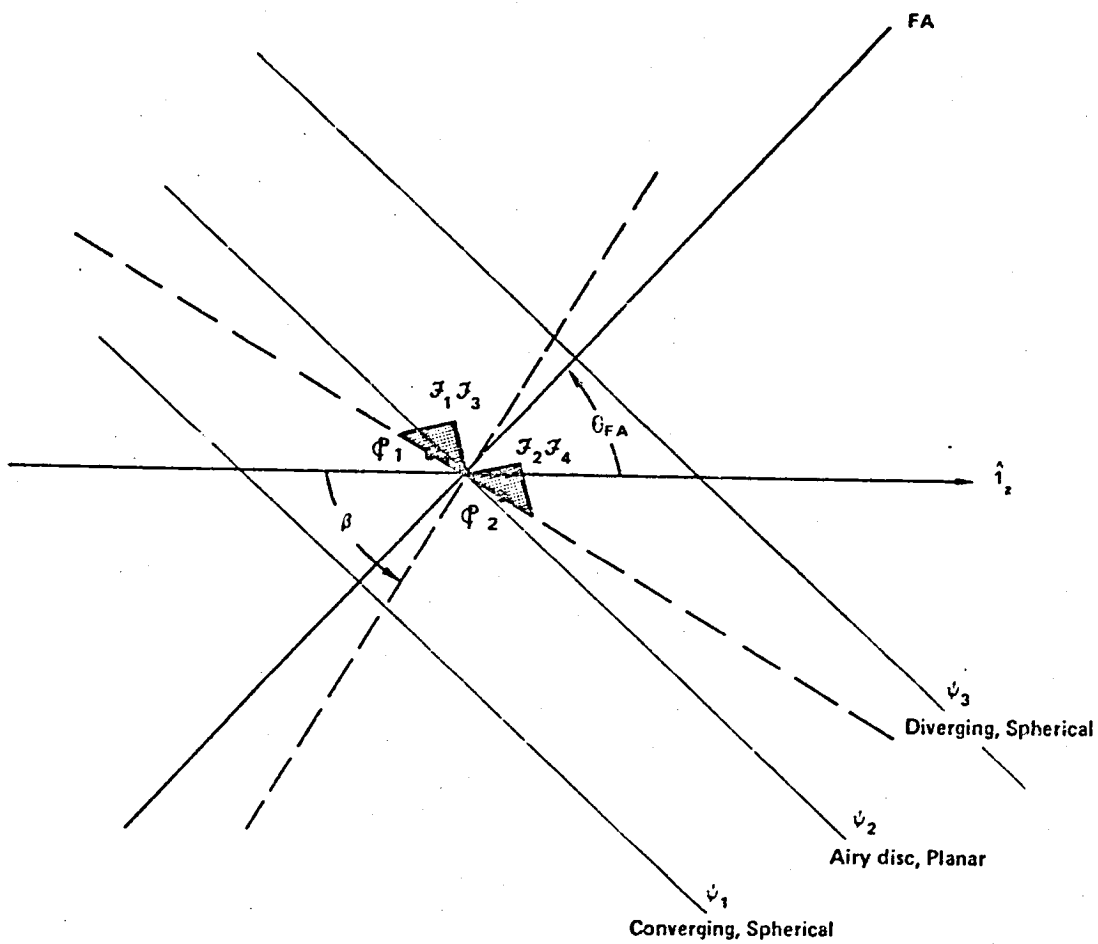


Figure 2. Wavefronts and Feeds in the Focal Region.

$$\Sigma = E_1 + E_2 + E_3 + E_4 \quad (2)$$

$$\Delta = (E_1 + E_3) - (E_2 + E_4). \quad (3)$$

The sum pattern can now be used to locate the focal point (F) by a standard procedure just as if it were a single feed. See Reference 1.

The phase center of the feed cluster in Figure 2 is at the geometric center of the cluster and is now assumed coincident with (F). For purposes of implementation, the separate sources (\mathcal{F}_1 - \mathcal{F}_4) may be taken of diameter $D_3 = \lambda/2$. The radius of the Airy disc, for a single reflector is

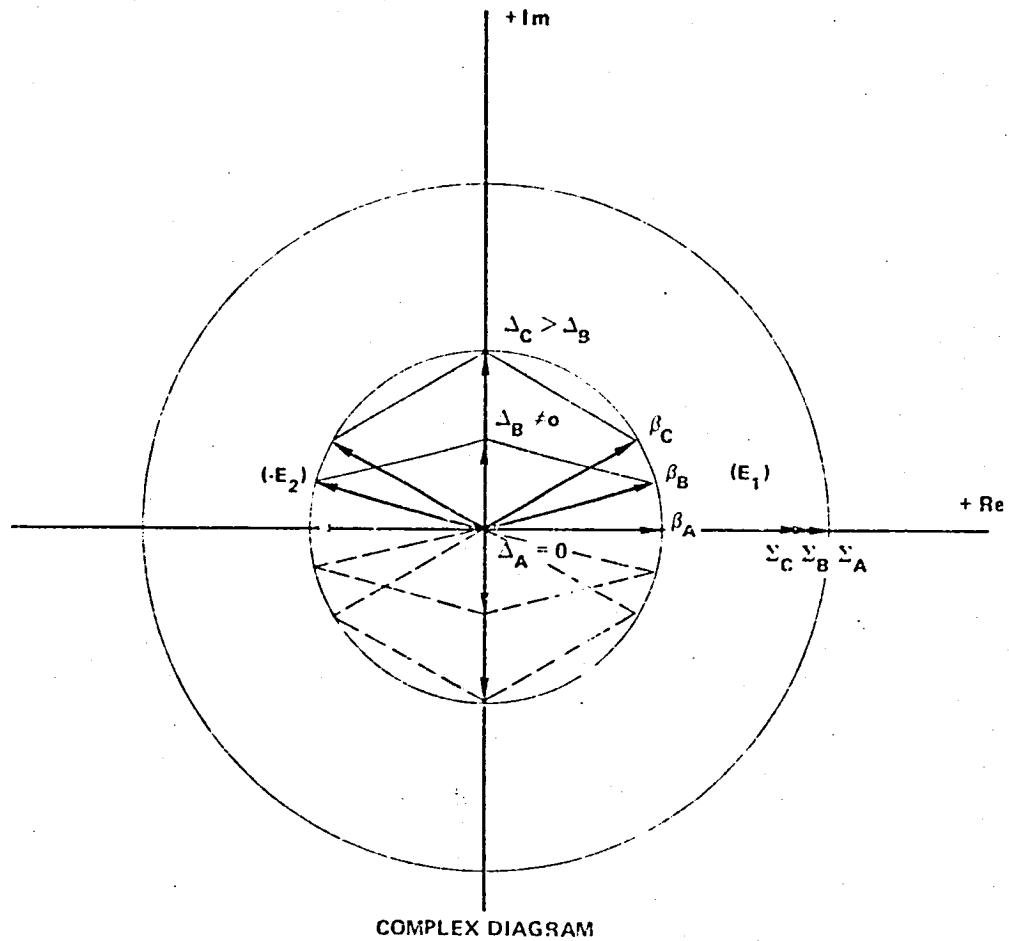
$$R_{AD} = \frac{1.22 F\lambda}{D} \quad (4)$$

where F and D are the focal length and aperture diameter of the offset reflector. The effect of cluster rotation on the difference pattern, under reception, is examined.

The outputs (Σ) and (Δ) of the comparator for resolving the single angle (θ_{FA}) are shown in the diagram of Figure 3. The sum (Σ) signal is arbitrarily situated on the positive real axis. It follows that the difference (Δ) signal is ideally either null, or temporally orthogonal to the (Σ) signal, a well known characteristic of phase-sensing monopulse configurations (PSM). Further, it appears that either the depth of the minima, corresponding to different cluster rotation angles (β), or the phase jump ($\sqrt{\pi L}$) can become criteria for resolving the focal axis angle (θ_{FA}), which is distinct from conventional monopulse techniques.

Even though monopulse is basically a receiving concept, reciprocity is now invoked and the far-field (Σ) and (Δ) radiation patterns are subsequently considered for mathematical simulation. Actually, only data corresponding to $\theta = 0^\circ$ are required; recall the previous discussion pertaining to reception of an axial plane wave. In the measurements realm, the far-field radiation patterns can, of course, be obtained two ways: (1) transmitter at the offset antenna, or (2) transmitter at a collimation tower. In the measurements approach $\theta = 0^\circ$ might not be directly identifiable; therefore, some small angular excursion to either side of $\theta = 0^\circ$ should be anticipated for the domain over which the (Σ) and (Δ) patterns are recorded. The transition from the detailed focal region field discussion to the far-field radiation patterns will subsequently be clarified by means of a specific example. The results obtained adhere closely to the theory presented above, but it may be more convincing to arrive at the orthogonality relationship illustrated in Figure 3 by reasoning through the sequence of events from the transmit point of view before proceeding with the example.

The feed configuration of Figure 2 is now combined with an offset paraboloid geometry such as that illustrated in Figure 1. Taken as an entity, this combination comprises a conventional amplitude-sensing monopulse configuration (ASM) when the feed cluster axis and the focal axis coincide ($\beta = \theta_{FA}$). When this coincidence is lacking, an errored amplitude-sensing monopulse configuration (cASM) may be identified. It is reasonable, therefore, to



(PSM)

Receive, PW @ $\theta = 0^\circ$

(fASM)

Transmit, SW \rightarrow PW (∞) @ $\theta = 0^\circ$

Figure 3. Sum ($E_1 + E_2$) and Difference ($E_1 - E_2$) Channel Signals for Feed Rotation Angles $\beta_A = \theta_{FA}$, $\beta_B > \theta_{FA}$, $\beta_C > \theta_{FA}$.

anticipate that the phase relationship for $\beta = \theta_{FA}$ between (Σ) and (Δ) is such that a phase jump or discontinuity (JEL) exists across $\theta = 0^\circ$. It is also reasonable to anticipate that the null value of the (Δ) channel associated with $\beta = \theta_{FA}$ will degrade to only a minimum value whose depth is a function of the angle (β) . This is because rotation of the feed axis away from the focal axis (1) reduces the transverse feed displacement component with respect to the focal axis, in turn reducing the amount of beam squint of the far-field radiation patterns and (2) increases the parallel feed displacement component, in turn introducing phase lead and phase lag of the individual squinted beam fields. See equations (5) and (6), under Radiation Pattern Data, for the feed displacement vectors $(\hat{\epsilon}_1)$ and $(\hat{\epsilon}_2)$.

The effects of feed cluster rotation may also be discussed in terms of reduced (\pm) linear phase gradients and increased (\pm) quadratic phase gradients in the aperture plane. The inference is that the lead-lag phase relationship between the fields of the separate squinted beams which are used to form the (Δ) pattern leads to the same situation depicted in Figure 3. In conclusion, regarding the offset paraboloid and the feed cluster as an entity on transmission, the (Σ) feed-cluster rotation introduces error into an amplitude-sensing monopulse configuration so that it acquires characteristics of a phase-sensing monopulse system.

RADIATION PATTERN DATA

The separate squinted radiation patterns which result from feed displacements such as those illustrated in Figure 2 are given as Figure 4. The vector displacements for a two-feed cluster are:

$$\hat{\epsilon}_1 = (x_{\epsilon_1}, y_{\epsilon_1}, z_{\epsilon_1}) = (R_g \cos \beta, 0.0, -R_g \sin \beta) \quad (5)$$

$$\hat{\epsilon}_2 = (x_{\epsilon_2}, y_{\epsilon_2}, z_{\epsilon_2}) = (-R_g \cos \beta, 0.0, R_g \sin \beta) \quad (6)$$

which is easily extended to a four-horn cluster. Figure 4 depicts the situation at $\beta_1 = \beta_2 = 52.0^\circ$. It is noted that there is a steep phase gradient across the main lobe of each beam which is attributable to the magnitude of the offset parameter for the parabolic surface. See Reference 2. The electromagnetic "center of gravity" is below the l_z axis, whereas the observer arc is centered on the origin of coordinates (o) and cuts across wavefronts as indicated by Figure 1.

The sum (Σ) and difference (Δ) far-field amplitude patterns corresponding to $\beta = \beta_1 = \beta_2 = 52^\circ, 54^\circ$, and 56° are shown as Figure 5, 6, and 7. Input parameters to the physical optics program which produced Figure 5 are:

Focal Length $F = 8.20208'$

Max. Radius $r_{max} = 6.56167'$

Min. Radius $r_{min} = 0.0'$

Offset Constants $x_{1p} = -8.85825', v_{1p} = 0.0', z_{1p} = -8.20208'$

Frequency $f = 37.0$ GHz

Wavelength $\lambda = 0.02658'$

Sampling Interval $l_i = 6.0$

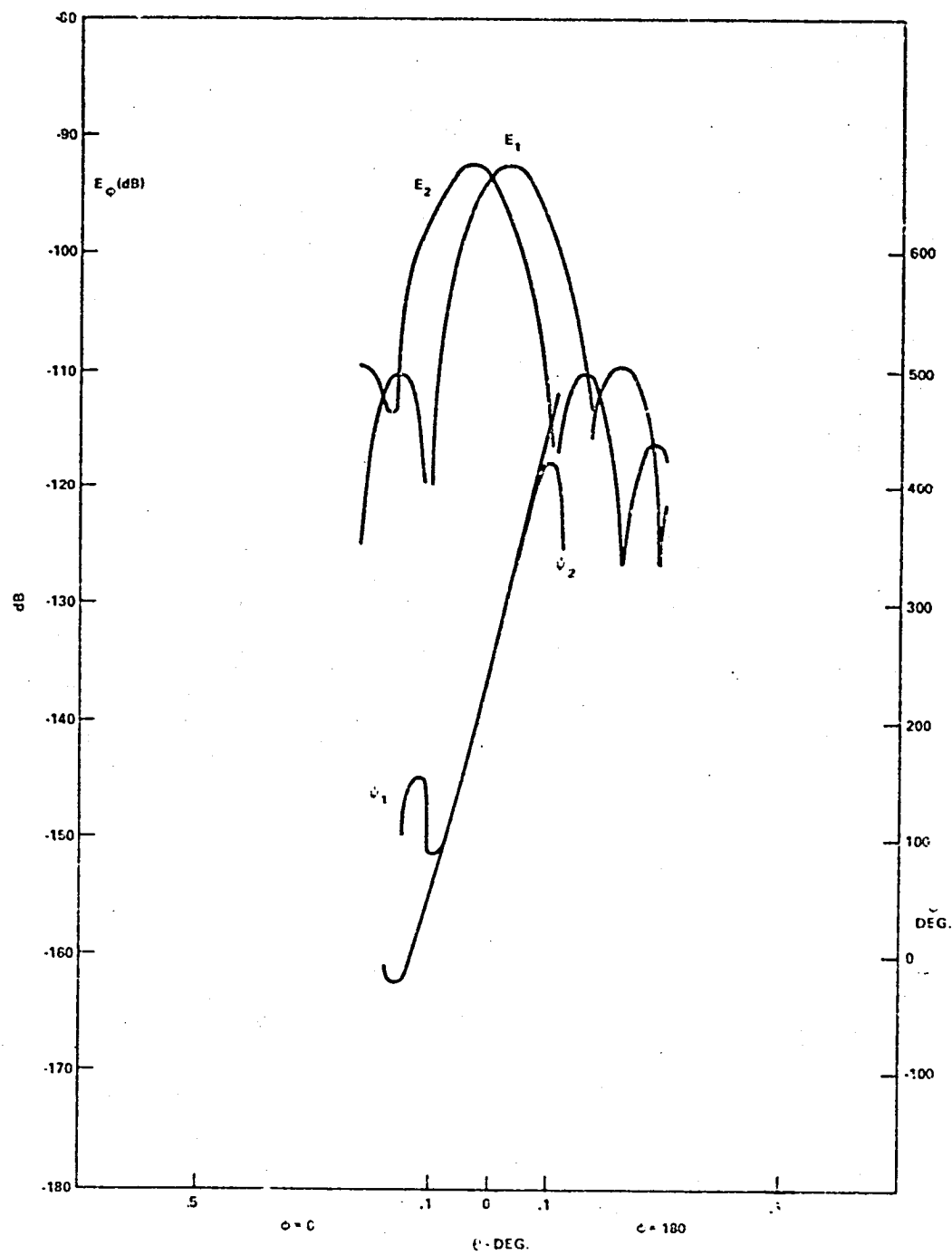


Figure 4. Squinted Beams of Feed Cluster ($\beta_{\mathfrak{Z}_1} = \beta_{\mathfrak{Z}_2} = 52^\circ$).

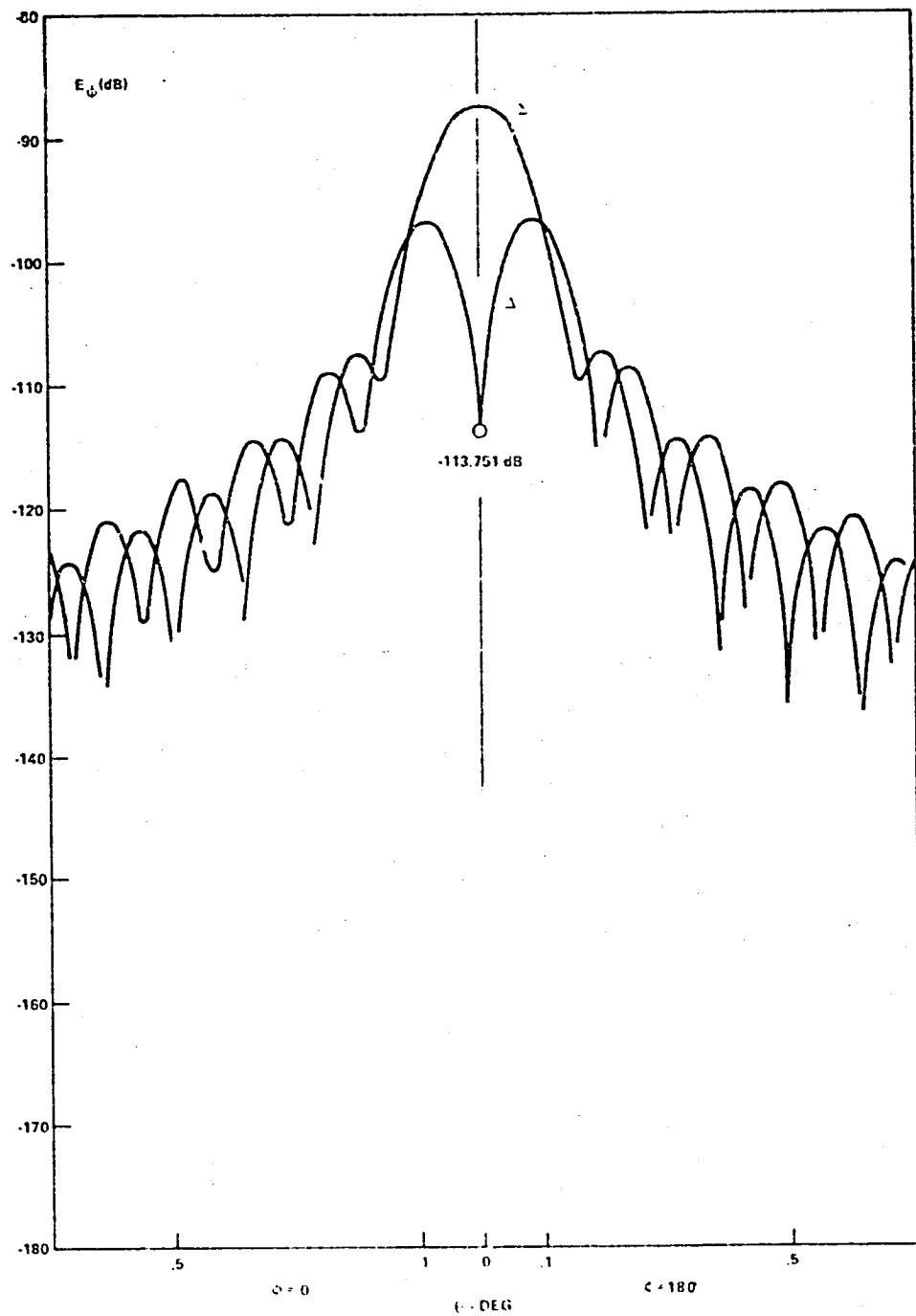


Figure 5. Sum and Difference Patterns ($\beta=52^\circ$).

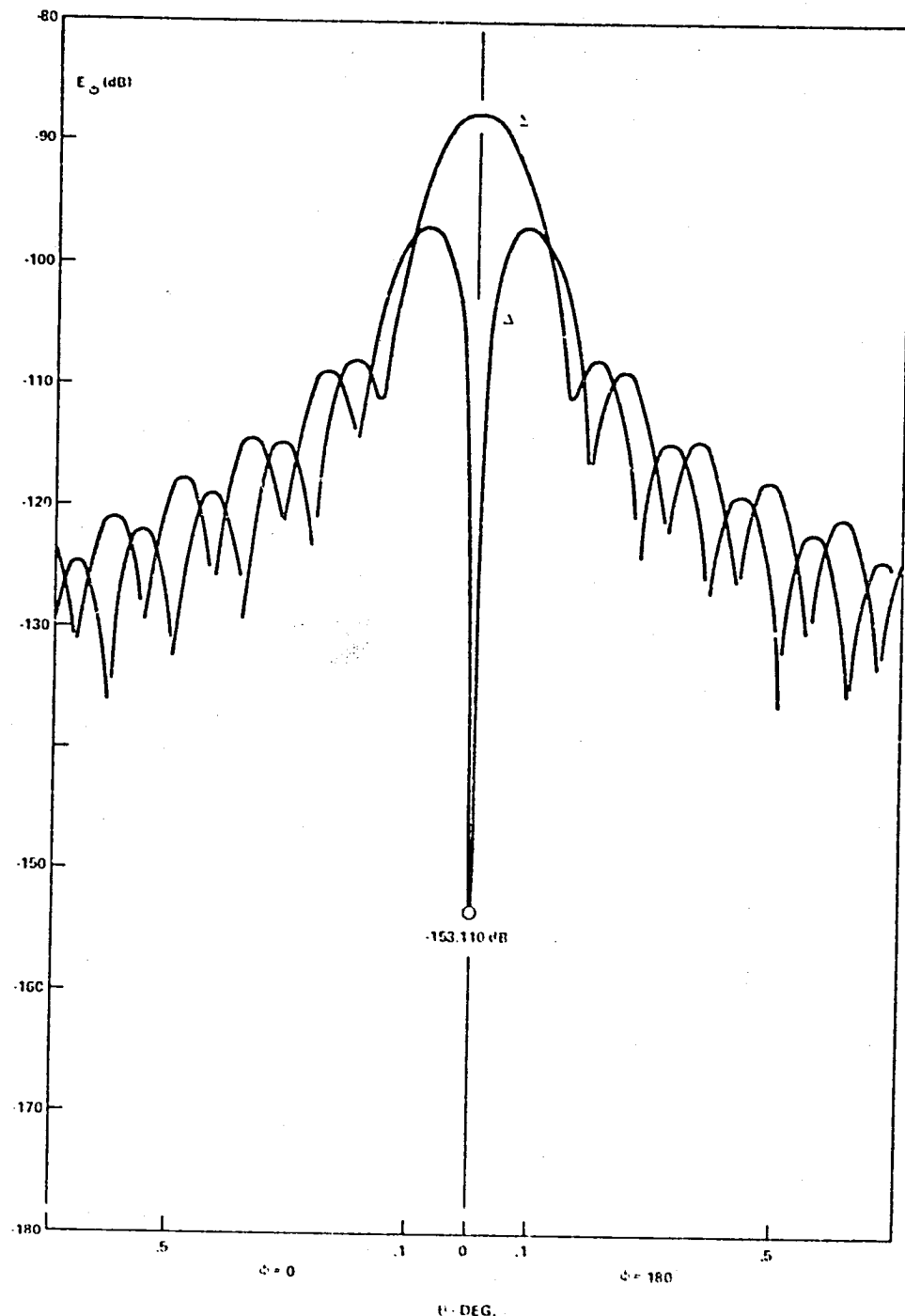


Figure 6. Sum and Difference Patterns ($\beta=54^\circ$).

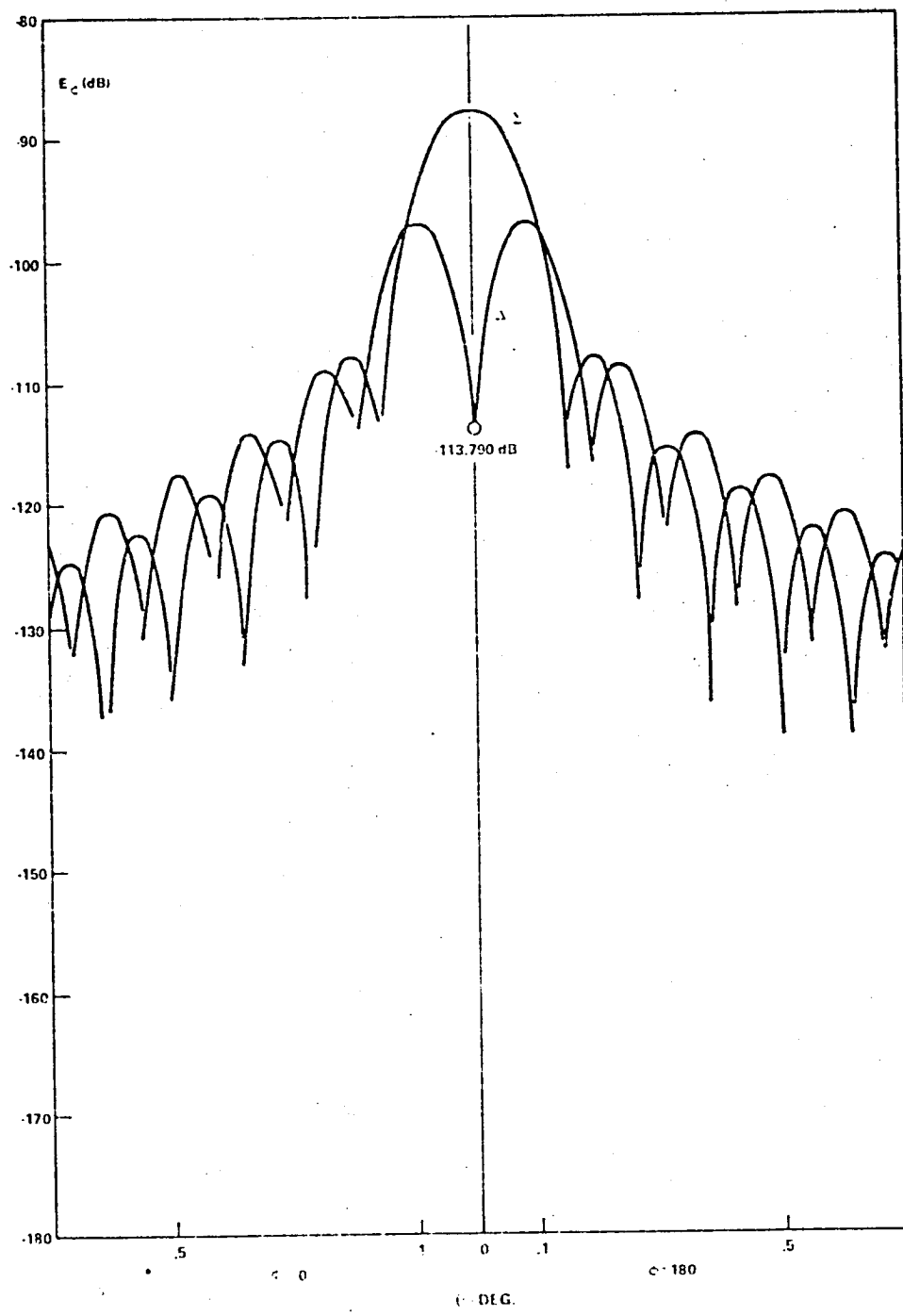


Figure 7. Sum and Difference Patterns ($\beta=56^\circ$).

Polarization Moments $P_1(I) = P_2(I) = 1.0$, $P_1(J) = P_2(J) = 0.0$
 $P_1(K) = P_2(K) = 0.0$

Feed Displacements $x_{\epsilon 1} = 0.00409'$, $y_{\epsilon 1} = 0.0'$, $z_{\epsilon 1} = -0.00524'$
 $x_{\epsilon 2} = -0.00409'$, $y_{\epsilon 2} = 0.0'$, $z_{\epsilon 2} = 0.00524'$

Euler Angles $\alpha_1 = 90^\circ$, $\beta_1 = 52^\circ$, $\gamma_1 = 0.0^\circ$, $\alpha_2 = 90^\circ$, $\beta_2 = 52^\circ$, $\gamma_2 = 0.0^\circ$

Exponent for Feed Pattern $E_J = \cos^N \theta$, $N_1 = 0.0$, $N_2 = 0.0$

and the parametric equations for the surface are:

$$x_p = \sigma_{\ell p} \sin \zeta_{\ell p} + x_{1p} \quad (7)$$

$$y_p = -\sigma_{\ell p} \cos \zeta_{\ell p} + y_{1p} \quad (8)$$

$$z_p = \frac{(\sigma p)^2}{4F} + z_{1p} \quad (9)$$

$$\sigma_p^2 = x_p^2 + y_p^2 \quad (10)$$

$$x_{1p} \neq 0 \Rightarrow \text{offset here} \quad (11)$$

$$y_{1p} \equiv 0 \text{ here} \quad (12)$$

$$z_{1p} = -F. \quad (13)$$

The anticipated null-filling can be seen in Figures 5, 6 and 7, with $\beta = 54^\circ$ emerging as the best estimate for the focal axis angle (θ_{FA}) of this set. Additional values of (β) were assumed, resulting in a composite plot of Δmin . versus β . See Figure 8.

Expanding the abscissa of Figure 8 by a factor of 100 and using small increments of (β) to obtain a more precise resolution of the focal axis angle (θ_{FA}) showed that the theoretical null could never be achieved with the offset paraboloid. Figure 9 converges to the zero derivative rather than the infinite derivative $\left(\frac{d \Delta \text{min}}{d \beta} \right)$. Nevertheless, the useful result $\theta_{FA} = 54.02^\circ$ is obtained

from Figure 9. The absence of a null is due to the asymmetry of the offset paraboloid as seen by the feeds (G_1) and (G_2) in Figure 2. It was found that the range of (β) values of Figure 9 resulted in squinted beam pairs such as shown in Figure 4 which crossed the $\tau = 0$ axis at slightly different levels. The deviation was between 0.0050 and 0.0054 dB. At $\beta = \theta_{FA}$ the far-field (A) patterns are antiphased, but can never annihilate perfectly. This is a characteristic of the $\phi = 0^\circ$, 180° radiation pattern cut for the offset paraboloid, but not the $\phi = 90^\circ$, 270° cut when the orthogonal error channel is implemented by feeds \mathcal{F}_3 and \mathcal{F}_n of Figure 2.

The sum (Σ) and difference (Δ) far-field phase patterns, obtained simultaneously in the physical optics solution with the amplitude patterns (Figures 5, 6, 7) are given here as Figures 10, 11, 12. Relative phase between (Σ) and (Δ) approaches a discontinuous jump π across $\theta = 0$ as β approaches θ_{FA} . A

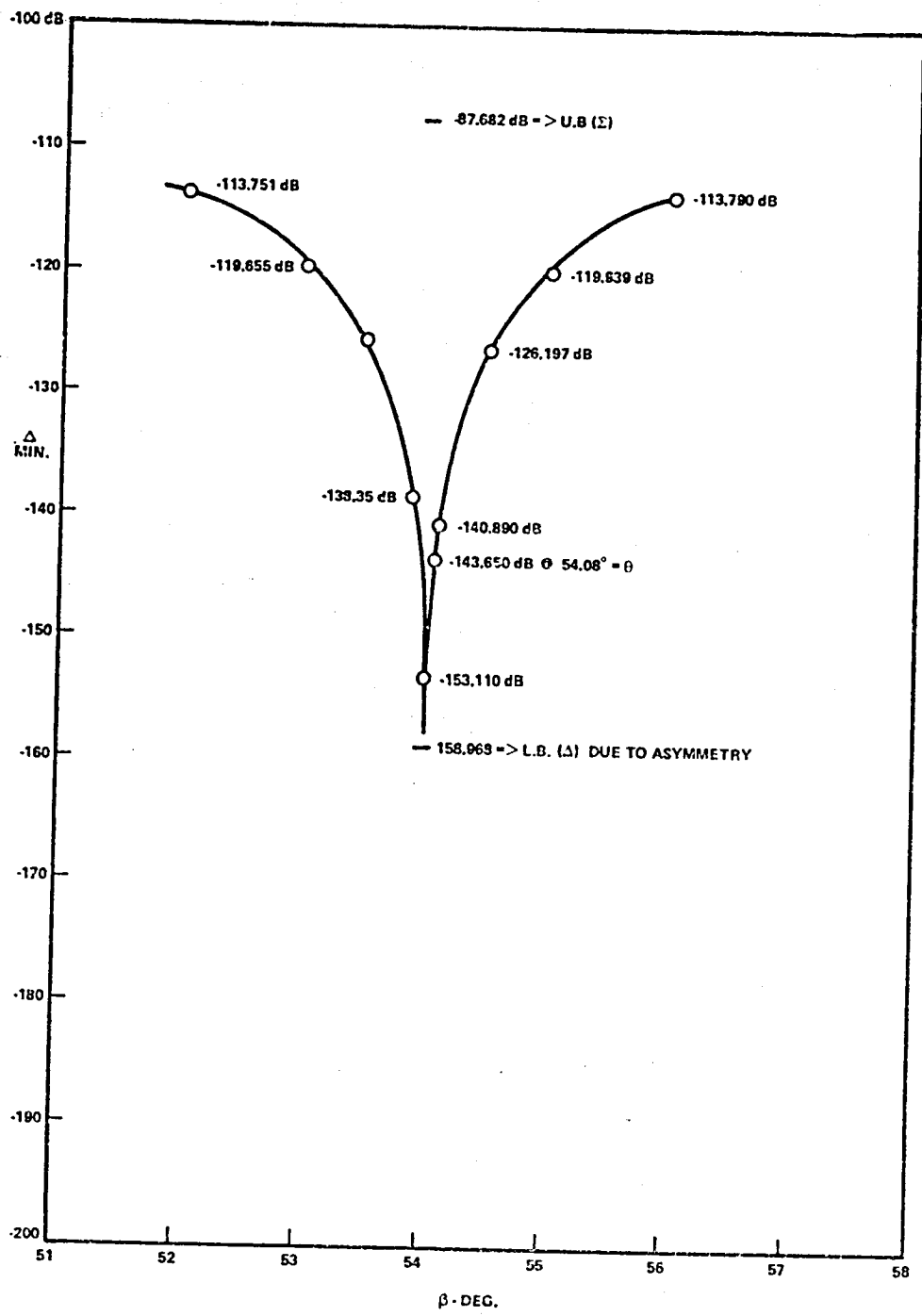


Figure 8. Difference Pattern Minima Versus Feed Cluster Rotation Angle (β).

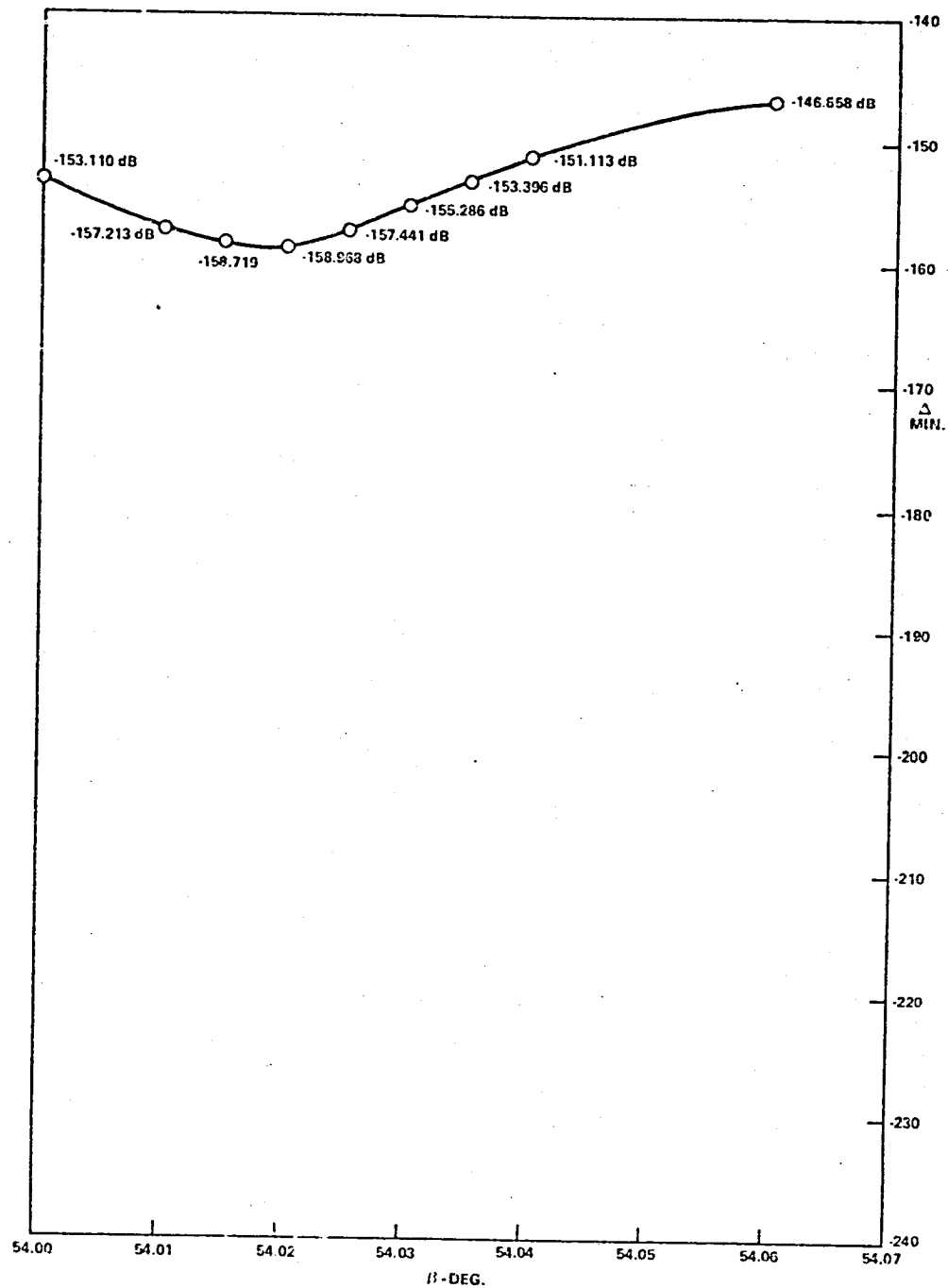


Figure 9. Difference Pattern Minima Versus Feed Cluster Rotation Angle (β).

composite plot is constructed and expanded as before. See Figures 13 and 14. It is apparent that these curves also lead to a precise resolution of the inclination angle (θ_{FA}) of the focal axis of the offset paraboloid. Whether amplitude or phase is used to determine this angle, the coarse scale allows direct reading to the nearest 0.10° and the expanded scale allows direct reading to the nearest 0.001° , well beyond most practical requirements.

Some of the features of Figures 10 through 12 are interesting and may be worth discussing. Their form is accounted for as follows. Under ideal conditions, ASM in an offset geometry exhibits relative phase difference equal to zero or π -radians, and a discontinuous jump ($\lfloor \pi \rfloor$) in the neighborhood of $\theta = 0^\circ$. See Figure 15. For this situation, the feed cluster axis coincides with the focal axis of the offset reflector ($\beta = \theta_{FA}$). In Figure 11, $\beta \approx \theta_{FA}$, and the ideal ASM characteristics are almost attained. The relative phase differences are approximately equal to zero or π radians away from $\theta = 0^\circ$. At $\theta = 0^\circ$ a relative phase difference of approximately $2\pi/3$ radians replaces a discontinuous jump $\lfloor \pi \rfloor$. In Figure 10 and Figure 12, β/θ_{FA} and relative phase differences vary noticeably as a function of observer angle (θ) and converge to $\pi/2$ radians at $\theta = 0^\circ$, which was predicted for (ASM), and is a characteristic usually associated with (PSM). The transition from (ASM) to (PSM) is very rapid as (β) approaches (θ_{FA}).

DUAL-ANGLE RESOLUTION

Two cases of dual-angle resolution are now considered. In the first case it is assumed that an ideal paraboloidal surface is retained, but both offset parameters are non-trivial. That is,

$$x_{1p} \neq 0 \quad (14)$$

$$y_{1p} \neq 0. \quad (15)$$

This is equivalent to a rotation or indexing of the previous single-angle resolution case since

$$(x_{1p}^2 + y_{1p}^2)^{\frac{1}{2}} = x_{1p} \quad (16)$$

dual	dual	single
------	------	--------

in general. A candidate focal axis is chosen as before, and either the minima of the (Δ) channel or the relative phase difference between the (Δ) and (Σ) channels may be used to resolve the focal axis (θ_{FA} , ϕ_{FA}) with precision. In the second case, it is assumed that the paraboloidal surface has undergone some perturbation possibly due to physical rotation of the mechanical structure or to solar distortion. The optical focal point (F) no longer exists, and is replaced by a caustic surface.

For the first case, a reasonable approximation to both θ_{FA} and ϕ_{FA} is assumed, since

$$0 \leq \phi_{FA} \leq 2\pi. \quad (17)$$

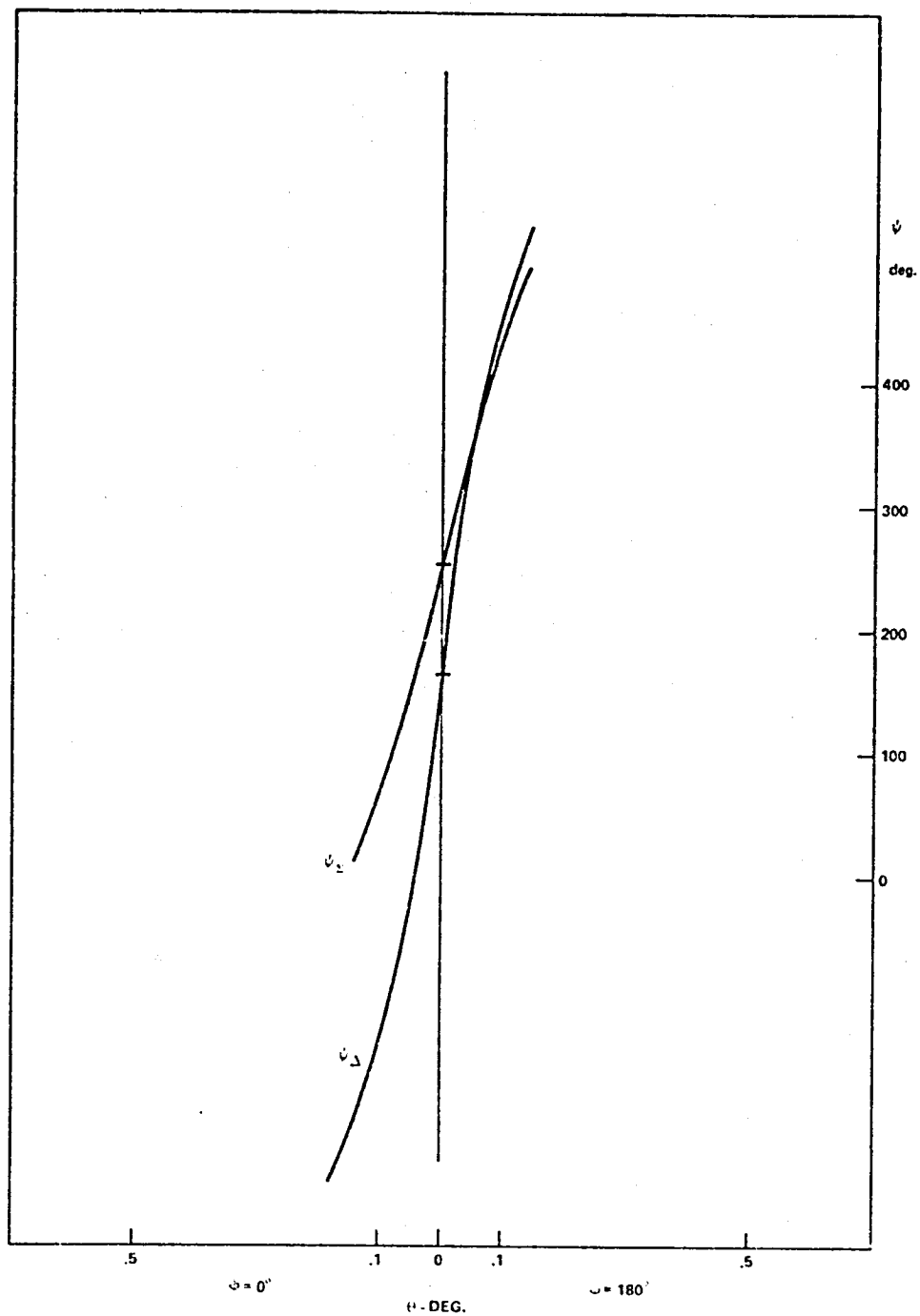


Figure 10. Sum and Difference Phase ($\beta=52^\circ$) Patterns.

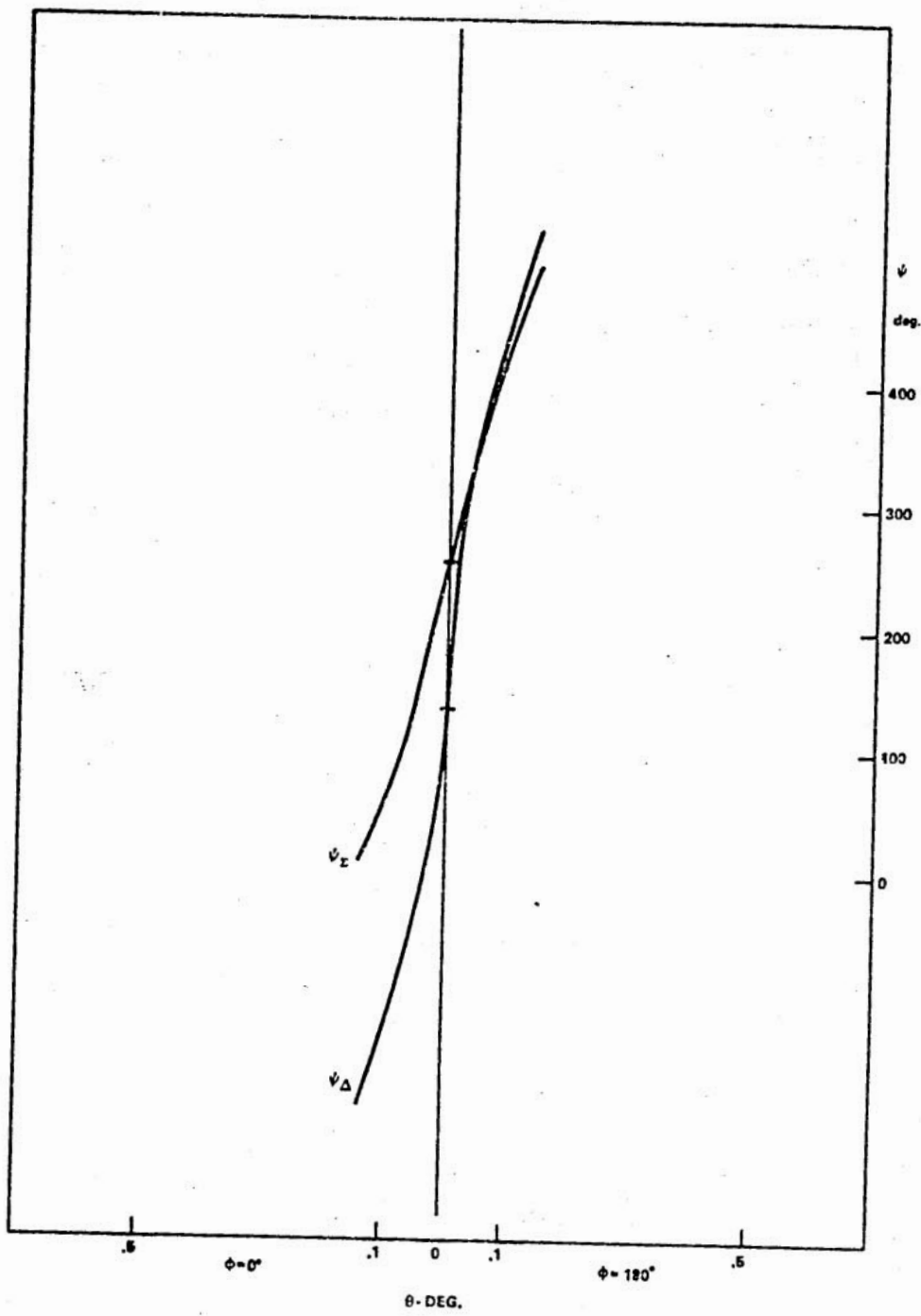


Figure 11. Sum and Difference Phase ($\beta=54^\circ$) Patterns.

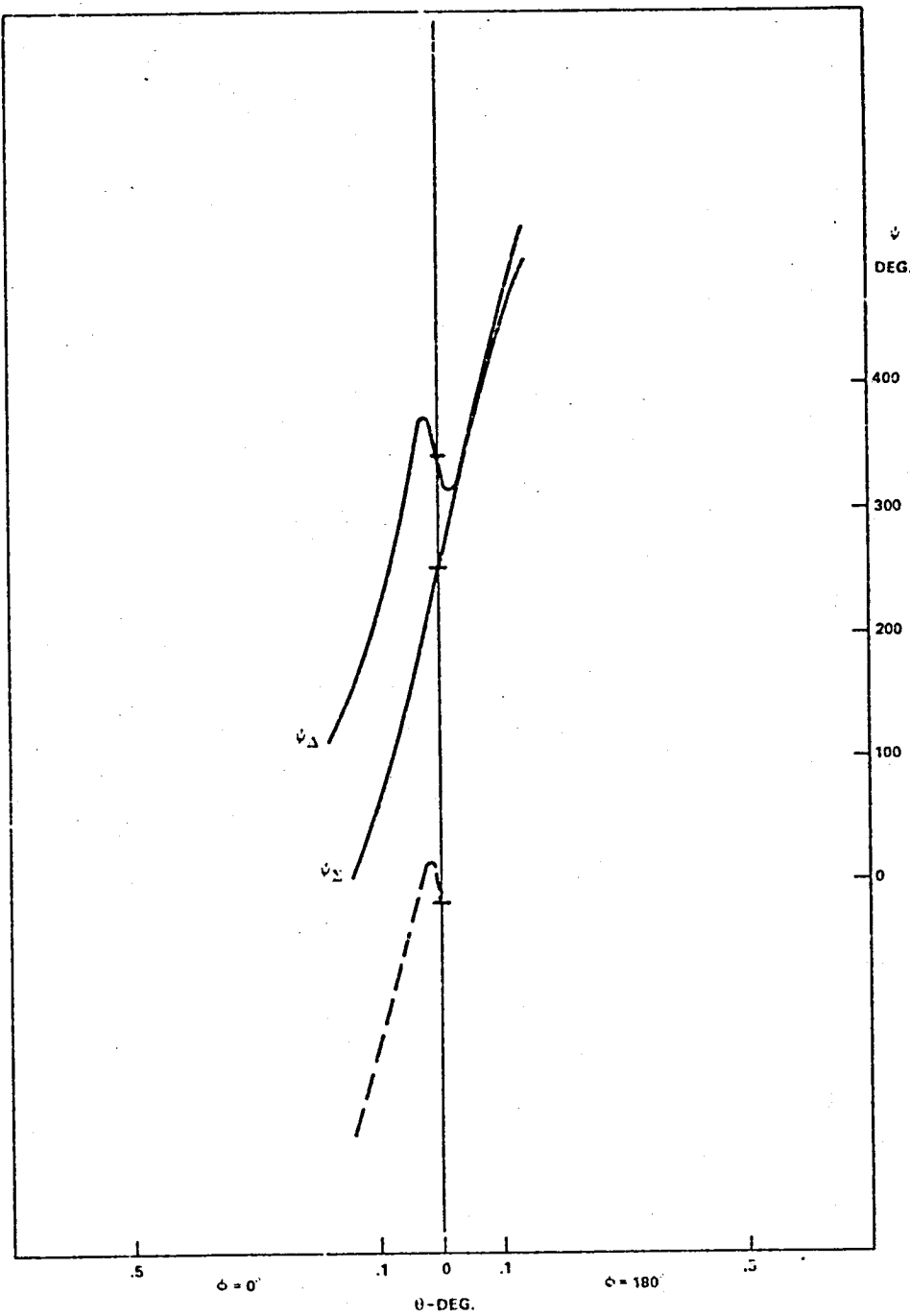


Figure 12. Sum and Difference Phase ($\beta=56^\circ$) Patterns.

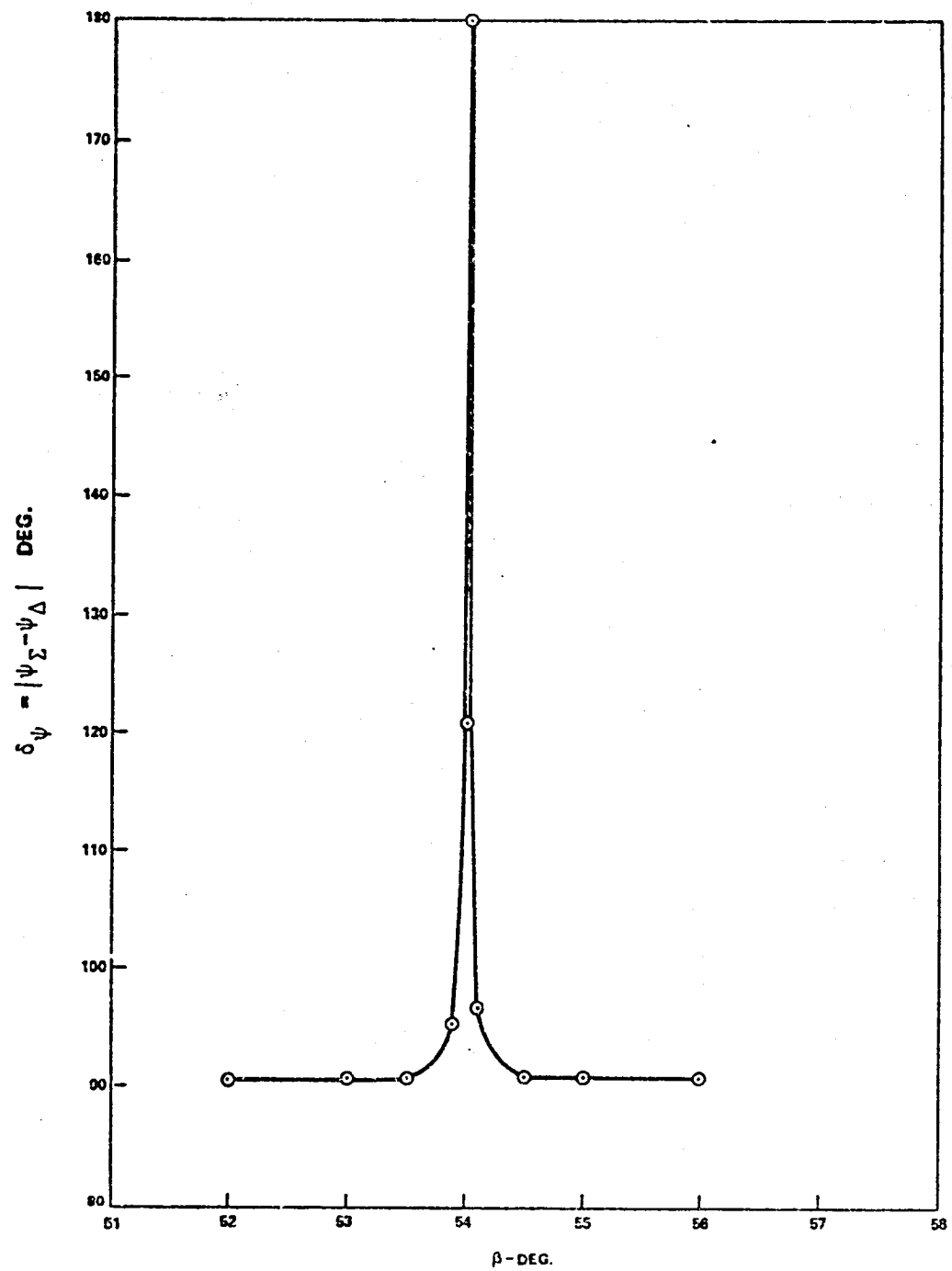


Figure 13. Relative Phase Difference $|\psi_{\Sigma} - \psi_{\Delta}|$, $\theta = 0^\circ$ Versus Feed Cluster Rotation Angle (β).

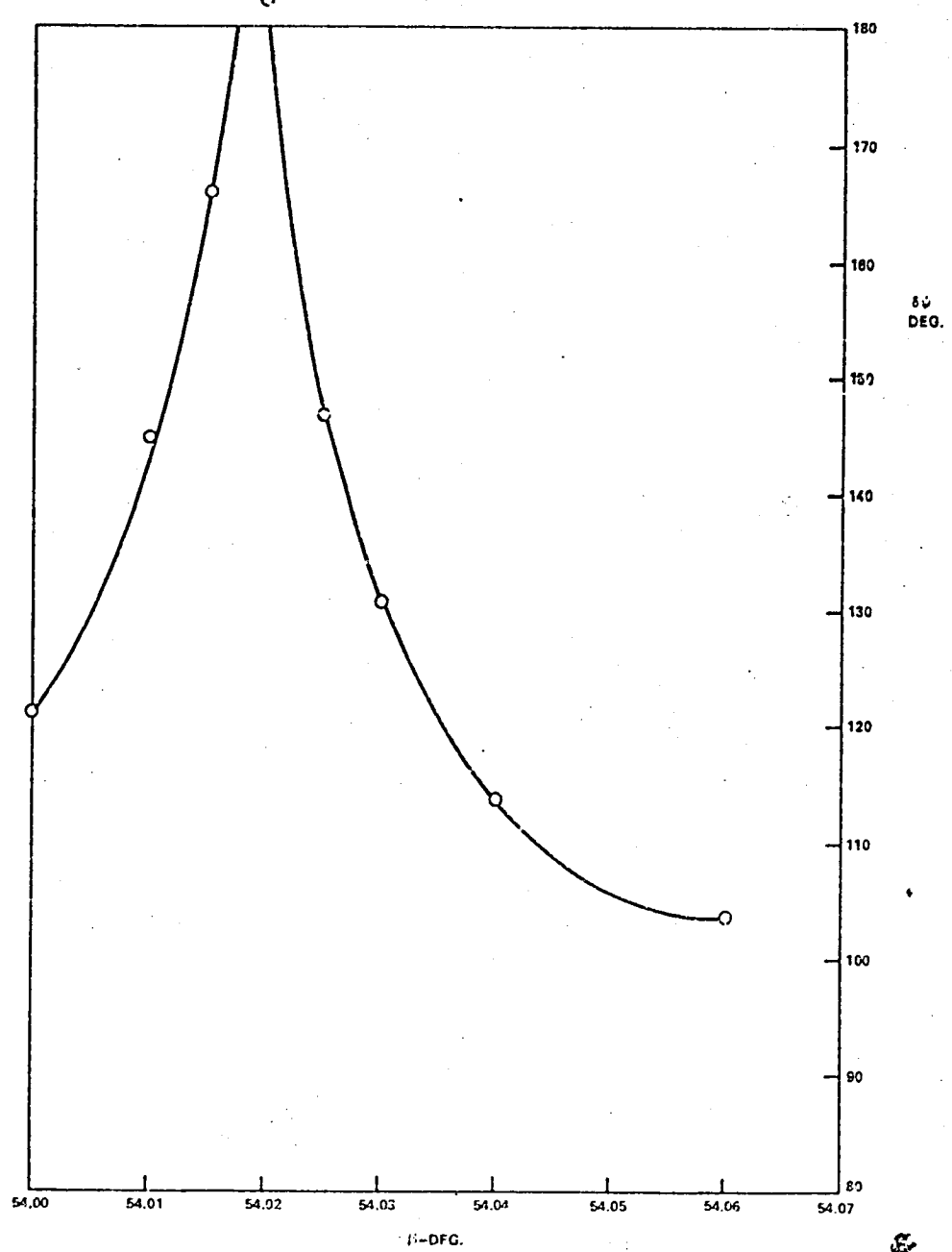


Figure 14. Relative Phase Difference $|\phi_2 - \phi_1|$, $\theta = 0^\circ$
Versus Feed Cluster Rotation Angle (θ).

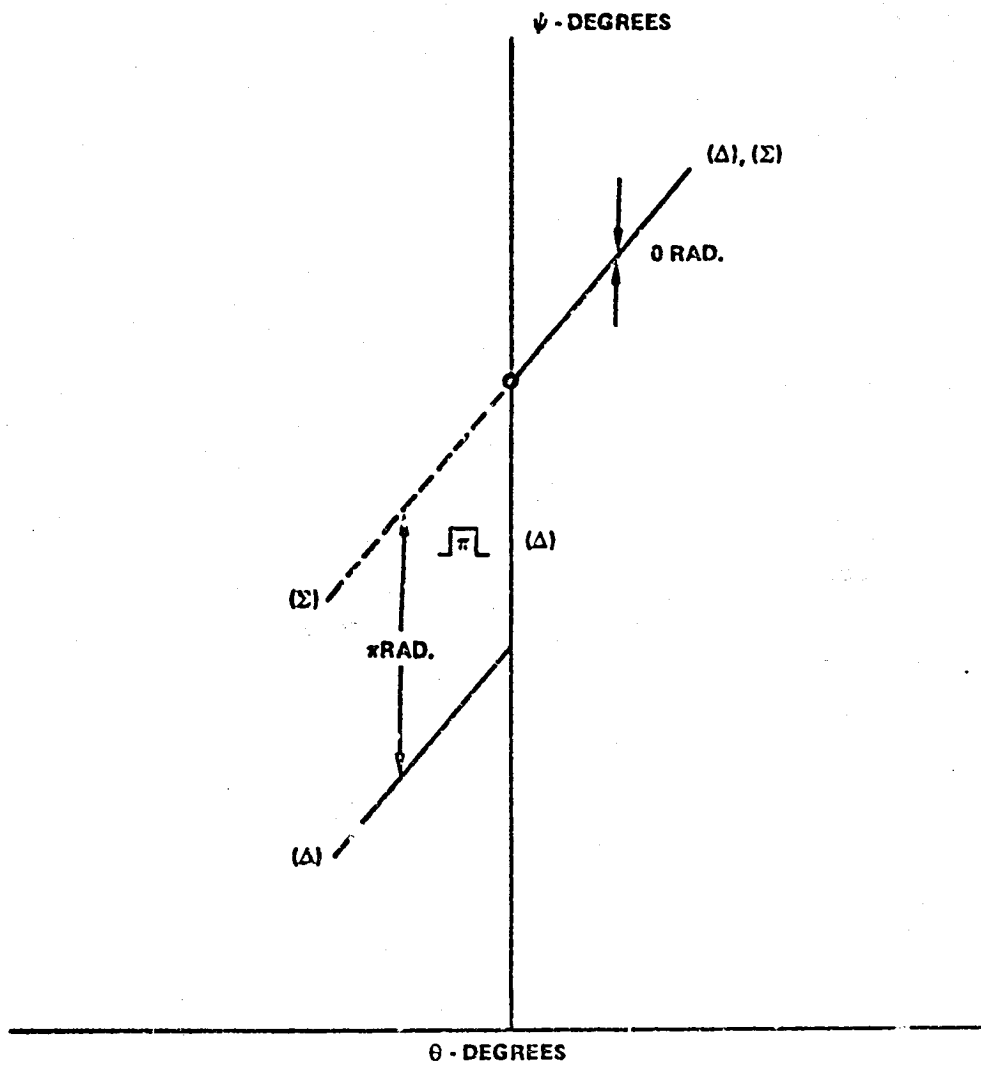


Figure 15. Phase Relationships for Offset Paraboloid (ASM).

For the second case, a reasonable approximation to θ_{FA} alone is required since it is obvious that

$$\phi \approx \pi \quad (18)$$

for $x_{IP} < 0$, the situation depicted in Figure 1. Also, it becomes necessary to admit other Euler angle values beside $\alpha = 90^\circ$, $\gamma = 0^\circ$ for the general feed cluster orientation, and two error channel signals are observed.

CONCLUSION

This TM has presented technical arguments leading to the conclusion that a single or dual-angle focal axis resolver, predicated on odd and even sensing functions, may be developed and applied in both mathematical simulation of antenna systems and in the physical world. An offset paraboloid, properly a sector of a parent or rotationally symmetric paraboloid, was used to illustrate the concepts. The focal axis resolver may be applied to other configurations as well. See Reference 4, which discusses the inclined focal axis of a dual parabolic cylinder antenna, for example.

In the course of the discussion, the terminology developed around phase-sensing and amplitude-sensing monopulse (PSM, ASM) was used. Reference to monopulse is natural here since certain aspects of the focal axis resolver discussion have a one-to-one correspondence with monopulse. Depending on what elements are encompassed and depending on the value of the feed cluster angle (β), errored ASM, pure ASM, and pure PSM can be identified. Conceptually, the introduction of a feed cluster in a focal region with planar wavefront tends to indicate that the resolver per se is a PSM device, the paraboloid functioning merely as a transducer which converts an incident plane wave into another (restricted) plane wave region. The utilization of the resolver, and reliance on the far field radiation patterns, dictate that the combination of feed cluster and paraboloid comprises either (eASM) or pure (ASM) is $\beta \neq \theta_{FA}$ or $\beta = \theta_{FA}$.

Actually, it can be argued that the focal axis resolver is neither (PSM), (eASM), or (ASM) since it is not imperative that the sum channel be used. The focal axis can be resolved by regarding the depth of the minimum of the error channel (ϵ) alone, which is not characteristic of monopulse operations. Target scintillation and noise would prohibit angle-tracking by this approach, and defeat the monopulse concept entirely. Further, the dependence on the development of several minima to determine the precise focal axis would be analogous to conical scanning rather than monopulse since a single pulse is inadequate to resolve a target bearing (α, γ) by the former method.

This TM has documented the rudiments of what appears to be a useful device for resolving focal axes with precision in difficult situations. Its limitations, implementation details, and techniques for eliminating feed and comparator errors through interchanges, for example, were not explored. Utilization of the resolver is in mathematical simulations, and in the physical world.

ACKNOWLEDGEMENTS

The author acknowledges discussions with, and background information from, Mr. J. L. King of Goddard Space Flight Center. The author is also greatly indebted to Mr. R. Miezis and Mr. J. Healy of Sigma Data Services Corporation who coded and applied the physical optics program used to develop the data in this TM. Finally, thanks are due Mr. L. R. Dod, Mr. R. Miezis, and Mr. J. Healy, the reviewers of the original manuscript who provided constructive criticism.

REFERENCES

1. Bartley, W. K., and Schmidt, R. F.; "Near-Field Antenna Focussing," X-811-75-184, Goddard Space Flight Center, August 1975.
2. Schmidt, R. F., "Focal Region Fields, Wavefronts, and Time-Average Poynting Vectors for a Large-Antenna Multiple-Frequency Microwave Radiometer (LAMMR)," TM-80647, Goddard Space Flight Center, March 1980.
3. Rhodes, D. R., "Introduction to Monopulse," McGraw-Hill Book Company, 1959.
4. Schmidt, R. F., "Parabolic-Cylinder Antennas," X-811-73-221, Goddard Space Flight Center, September 1973.

APPENDIX A
Rim and Aperture Boundaries

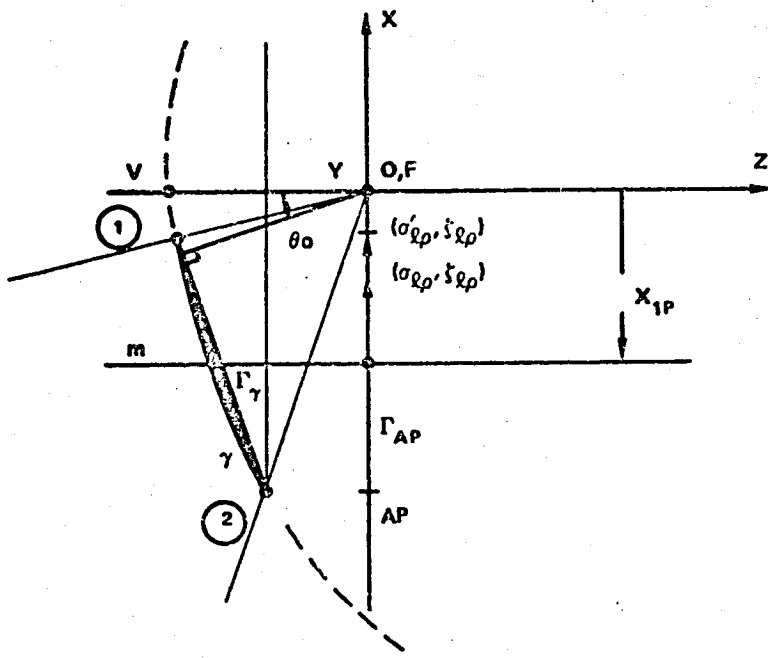


Figure A-1. Offset Paraboloid.

From Figure A-1 it can be seen that for every point $(\sigma'_{lp}, \zeta_{lp})$ of a polar net coincident with the aperture plane (AP) there exists a point on the surface γ . If, in particular, only a circular rim of the aperture (Γ_{AP}) is considered, it follows that only the physical rim (Γ_γ) of the surface is obtained. Then the entire set of rim points (x'_p, y'_p, z'_p) or (Γ_γ) may be written as the entire set of rim points

$$x'_p = \sigma'_{lp} \sin \zeta_{lp} + x_{1p} \quad (1-A)$$

$$y'_p = -\sigma'_{lp} \cos \zeta_{lp} + y_{1p} \quad (2-A)$$

$$z'_p = \frac{(\sigma'_{lp})^2}{4F} + z_{1p} \quad (3-A)$$

$$(\sigma'_{lp})^2 = (x'_p)^2 + (y'_p)^2 \quad (4-A)$$

where

$$x_{1p} \neq 0 \Rightarrow \text{offset here} \quad (5-A)$$

$$y_{1p} = 0 \quad (6-A)$$

$$z_{1p} = -F \quad (7-A)$$

and $(\sigma' \ell_p)$ designates the aperture radius value. The collection of points (x'_p, y'_p, z'_p) constitutes the intersection of a cylinder with a paraboloid, the axes of both rotationally symmetric surfaces being assumed parallel, but not in general coincident.

A method of demonstrating that the rim (Γ_γ) of the physical surface is an ellipse is to first establish that it is a planar curve. A rotational transformation about the y-axis of Figure A-1 accomplishes this, and the amount of that rotation (θ_o) is determined here by the rim points corresponding to $\zeta_{lp} = 90^\circ, 270^\circ$. The rotational transformation is

$$x = x'_p \cos \theta_o - z'_p \sin \theta_o \quad (8-A)$$

$$y = y'_p \quad (9-A)$$

$$z = x'_p \sin \theta_o + z'_p \cos \theta_o \quad (10-A)$$

and the angle is

$$\theta_o = \text{arc tan} \frac{|\Delta z|}{|\Delta x|} = \frac{z'_{(2)} - z'_{(1)}}{x'_{(1)} - x'_{(2)}} = \frac{-x_{1p}}{2F} \quad (11-A)$$

Since the latter establishes that

$$\sin \theta_o = -x_{1p} / [(x_{1p})^2 + (4F^2)]^{1/2} \quad (12-A)$$

$$\cos \theta_o = 2F / [(x_{1p})^2 + (4F^2)]^{1/2}, \quad (13-A)$$

the rotated rim (Γ_γ) appears as

$$x = \frac{(\sigma' \ell_p \sin \zeta_{lp} + x_{1p}) 2F}{(x_{1p}^2 + 4F^2)^{1/2}} - \frac{[z'] (-x_{1p})}{(x_{1p}^2 + 4F^2)^{1/2}} \quad (14-A)$$

$$y = -\sigma'_{\ell p} \cos \zeta_{\ell p} \quad (15-A)$$

$$z = \frac{(\sigma'_{\ell p} \sin \zeta_{\ell p} + x_{1p}) (-x_{1p})}{(x_{1p}^2 + 4F^2)^{\frac{1}{2}}} + \frac{[z'] (2F)}{(x_{1p}^2 + 4F^2)^{\frac{1}{2}}} \quad (16-A)$$

where

$$[z'] = \frac{(\sigma'_{\ell p})^2}{4F} - F = \frac{[(x')^2 + (y')^2]}{4F} - F$$

$$= \frac{(\sigma'_{\ell p})^2 + 2x_{1p} \sigma'_{\ell p} \sin \zeta_{\ell p} + x_{1p}^2}{4F} - F \quad (17-A)$$

Substituting [z'] into (15-A) leads to

$$z = [-\frac{1}{2} x_{1p}^2 - \frac{1}{2} (\sigma'_{\ell p})^2 - 2F^2] / (x_{1p}^2 + 4F^2)^{\frac{1}{2}} = \text{constant.} \quad (18-A)$$

Since (18-A) is independent of ($\zeta_{\ell p}$), and $\sigma_{\ell p} = \sigma'_{\ell p} = \text{constant}$, as well as (x_{1p}) and (F), it may be concluded that the physical rim of the offset paraboloid, which was designated (Γ_y), is a planar curve. That is, the intersection of a cylinder with axis parallel to the parent paraboloid axis lies in a plane.

From equations (14-A) and 15-A) which relate to a planar curve,

$$x = \frac{\left\{ [(\sigma'_{\ell p})^2 - (y)^2]^{\frac{1}{2}} + x_{1p} \right\} 2F}{(x_{1p}^2 + 4F^2)^{\frac{1}{2}}} - \left\{ \frac{(\sigma'_{\ell p})^2 + 2x_{1p} [(\sigma'_{\ell p})^2 - (y)^2]^{\frac{1}{2}}}{4F} - F \right\} \frac{(-x_{1p})}{(x_{1p}^2 + 4F^2)^{\frac{1}{2}}} \quad (19-A)$$

After some algebraic reduction,

$$x = \frac{2[(\sigma'_{\ell p})^2 - (y)^2]^{\frac{1}{2}} (x_{1p}^2 + 4F^2) + x_{1p} (x_{1p}^2 + 4F^2) + x_{1p} (\sigma'_{\ell p})^2}{4F(x_{1p}^2 + 4F^2)^{\frac{1}{2}}} - \quad (20-A)$$

which is recognized as the equation of an ellipse. Letting

$$C_o = (x_{1P}^2 + 4F^2)^{\frac{1}{2}} = \text{constant} \quad (21-A)$$

the standard form of an ellipse is easily recovered:

$$\frac{\left[x - x_{1P}[(C_o)^2 + (\sigma' l_p)^2] \right]^2}{4C_o F} + \frac{y^2}{\left(\frac{C_o \sigma' l_p}{2F} \right)^2} = 1 \quad (22-A)$$

When $x_{1P} \rightarrow 0$, the ellipse degenerates to a circle.

BIBLIOGRAPHIC DATA SHEET

1. Report No. TM 80683	2. Government Accession No.	3. Recipient's Catalog No.	
4. Title and Subtitle Focal Axis Resolver for Offset Reflector Antennas		5. Report Date May 1980	
7. Author(s) R. F. Schmidt		6. Performing Organization Code 946	
9. Performing Organization Name and Address NASA Goddard Space Flight Center Greenbelt, Md. 20771		8. Performing Organization Report No.	
12. Sponsoring Agency Name and Address National Aeronautics and Space Administration Washington, D.C. 20546		10. Work Unit No.	
		11. Contract or Grant No.	
		13. Type of Report and Period Covered Technical Memorandum	
		14. Sponsoring Agency Code	
15. Supplementary Notes			
16. Abstract This document describes electrical means for determining the focal axis of an offset reflector antenna whose physical rim is not coincident with the boundary of the electrical aperture. Even and odd sensing functions are employed in the focal region, leading to both amplitude and phase criteria for restoring a focal axis generally inclined with respect to the system axis. The analytical aspects of the problem are discussed and an example related to a 4-meter Large-Antenna Multiple-Frequency Microwave Radiometer (LAMMR) is included. It is shown that the technique is useful for focal axis determination in mathematical situations and in the physical world.			
17. Key Words (Selected by Author(s)) Antenna, Microwave, Offset Paraboloid, Focal Axis Resolver		18. Distribution Statement Unclassified-Unlimited	
19. Security Classif. (of this report) Unclassified	20. Security Classif. (of this page) Unclassified	21. No. of Pages 35	22. Price* \$4.50

*For sale by the National Technical Information Service, Springfield, Virginia 22151.

GSFC 25-44 (10/77)

END

DATE

FILMED

SEP 8 1980



3 1176 00020 5493